

Learning to Balance: Decoupled Siamese Diffusion Transformer for Reference-Based Remote Sensing Image Super-Resolution

Bin Luo¹, Runmin Dong^{2*}, Zhaoyang Luo¹, Jinxiao Zhang⁴,
Jiyao Zhao³, Fan Wei⁴, and Haohuan Fu^{1,3*}

¹ Tsinghua Shenzhen International Graduate School, Shenzhen, China

² Sun Yat-sen University, Zhuhai, China

³ National Supercomputing Center in Shenzhen, Shenzhen, China

⁴ Tsinghua University, Beijing, China

luob21@mails.tsinghua.edu.cn, dongrm3@mail.sysu.edu.cn

Abstract. Diffusion-based methods demonstrate significant potential for remote sensing image super-resolution at large scaling factors, particularly in reference-based super-resolution (RefSR) where high-resolution reference images provide critical fine-grained texture priors. However, existing methods often suffer from a trade-off between over-reliance on reference information, which leads to texture artifacts, and underutilization, which results in insufficient detail recovery. To address these issues, we propose DS-DiT, a Decoupled Siamese Diffusion Transformer method that decouples low-resolution and reference interactions at the attention level. By enabling low-resolution structural priors and reference texture information to interact independently with the noisy latent, the framework effectively mitigates inter-source competition. Furthermore, to compensate for the limited local modeling ability of global attention, we introduce a Patch-Level Weights (PLW) module that adaptively modulates the fusion of conditional sources. In addition, this siamese architecture facilitates an autoguidance strategy during inference, which enhances reconstruction by exploiting the prediction discrepancy between strong and weak reference conditions. This approach boosts generation quality without additional training. Experimental results across multiple datasets and scaling factors demonstrate that DS-DiT outperforms existing methods in both quantitative metrics and visual fidelity. The code is available at <https://github.com/Binary-L/DS-DiT>.

Keywords: Image Super-Resolution · Diffusion Model · Remote Sensing

1 Introduction

High-resolution (HR) remote sensing (RS) imagery is indispensable for a wide range of applications, including urban planning, environmental monitoring, and

* Corresponding authors

disaster assessment [6, 16]. However, due to inherent constraints in sensor hardware and imaging conditions, acquired RS images often suffer from a trade-off between spatial and temporal resolutions [25], frequently failing to meet the requirements of fine-grained analysis. Image super-resolution (SR) techniques have emerged as an effective solution to bridge this gap by reconstructing HR images from easily accessible low-resolution (LR) observations with short revisit cycles, thereby effectively filling the temporal gaps in high-resolution data sequences.

Despite their utility, single-image super-resolution (SISR) methods face severe ill-posedness at large scaling factors [49], such as $\times 8$ or $\times 16$, where they struggle to accurately recover lost high-frequency details. Reference-based super-resolution (RefSR) addresses this limitation by introducing an additional HR reference (Ref) image from the same geographic area but at a different acquisition time. The rich texture priors provided by these reference images effectively alleviate the information deficiency inherent in SISR. While LR and Ref images are typically multi-temporal observations of the same location and share aligned spatial extents, factors such as varying viewpoints, spectral differences, and land cover changes make the effective exploitation of reference features challenging. Consequently, early RefSR methods [17, 51] focused primarily on feature alignment between LR and Ref to facilitate the transfer of reference textures.

The emergence of diffusion models [26, 47] has revolutionized RS RefSR by introducing multi-condition generative frameworks. Although diffusion models can generate remarkably rich details, especially by leveraging reference textures, they are prone to over-reliance on Ref features, which often leads to artifacts or false textures. Therefore, the core challenge in RS RefSR lies in effectively utilizing reference textures in unchanged regions while suppressing erroneous transfers in areas where land cover has changed. To this end, methods like Ref-Diff [7] introduce ideal land cover change priors as explicit conditions to guide the diffusion process. However, the performance of such methods degrades significantly in real-world applications where precise change detection masks are unavailable. Even the joint use of independent change detection and diffusion models often fails to produce stable and high-quality super-resolution results.

Meanwhile, the state-of-the-art in generative modeling has shifted toward Multimodal Diffusion Transformer (MM-DiT) architectures [10, 20], which achieve superior fusion through joint self-attention mechanisms. Nevertheless, for RS imagery, the standard text modality is insufficient for describing complex land cover features, rendering traditional text-guidance mechanisms ineffective. The optimal architectural design for integrating high-resolution reference images within the MM-DiT framework remains an open research challenge. A straightforward approach would be to replace the text branch in MM-DiT with LR and Ref images as new conditioning modalities. However, we observe that unconstrained interaction among these conditions leads to information competition, causing certain features to be over-exploited or under-utilized.

To mitigate these issues, and drawing inspiration from the architectural paradigms explored in CreatiLayout [45] and TODSynth [42], we propose DS-DiT, a Decoupled Siamese Diffusion Transformer method that decouples LR and

Ref interactions at the attention level. Unlike existing siamese designs that replicate noisy features, our design allows the noisy image tokens to generate a single shared set of query, key, and value (Q, K, and V) matrices that are dispatched to two parallel joint attention paths. This configuration ensures that LR structural priors and Ref texture information interact independently yet consistently with the same noisy image latent, effectively alleviating inter-source competition while maintaining global coherence. Furthermore, global attention mechanisms may overlook critical local details. To address this, we introduce a Patch-Level Weights (PLW) module that adaptively regulates the fusion of multi-source information, enhancing fine-grained detail recovery.

Importantly, by allowing the noisy image tokens to generate a single shared set of Q, K, and V, our decoupled siamese architecture provides a consistent latent anchor for the parallel attention paths. This consistency allows us to introduce an autoguidance strategy during inference, which is analogous to classifier-free guidance [14]. By exploiting the prediction discrepancy of the same model under strong and weak reference conditions, we explicitly amplify reference utilization and boost generation quality without the need for additional training or auxiliary models. Extensive experiments on two benchmark datasets across large scaling factors demonstrate that DS-DiT achieves superior results even in the absence of ideal change detection priors.

The main contributions of this work are summarized as follows:

- We propose a Decoupled Siamese Diffusion Transformer (DS-DiT), which mitigates inter-source information competition by decoupling LR and Ref interactions at the attention level. This decoupled architecture further enables an inference-time autoguidance strategy, which boosts generation quality without requiring additional training or auxiliary models.
- We design a Patch-Level Weights (PLW) module to adaptively modulate the fusion of structural and texture features on a per-patch basis. By mitigating the detail loss inherent in global attention, this module enhances fine-grained detail recovery.
- Extensive experiments on the SECOND and FUSU datasets demonstrate that DS-DiT outperforms state-of-the-art methods in both quantitative metrics and visual fidelity at large scaling factors of $\times 8$ and $\times 16$.

2 Related Work

2.1 Reference-Based Image Super-Resolution

Compared to single-image super-resolution (SISR), RefSR achieves higher-quality reconstruction by jointly exploiting a low-resolution (LR) image and an additional high-resolution reference (Ref) image. Early RefSR methods focus primarily on feature alignment between the LR and reference images to enable texture transfer. CrossNet [51] employs optical flow estimation for image alignment, while SRNTT [50] performs multi-scale matching in the feature space. TTSR [39] transfers textures via cross-attention, and AMSA [38] adopts a coarse-to-fine

progressive matching strategy. C²-Matching [17] leverages contrastive learning and knowledge distillation to handle cross-transformation and cross-resolution matching. DATSR [3] further introduces deformable attention for more flexible feature alignment.

Unlike natural images, the LR and Ref images in remote sensing scenarios are typically acquired from the same location at different times, and can thus be considered spatially aligned. Consequently, the core challenge of remote sensing RefSR lies in effectively exploiting reference textures in unchanged regions while suppressing the erroneous transfer of irrelevant textures in changed regions. However, existing remote sensing RefSR approaches [8, 46] remain insufficient in utilizing effective texture information from Ref images. At large scaling factors, GAN-based methods struggle to faithfully reconstruct fine details in changed regions, leading to reconstructed images that lack high-frequency details. While recent diffusion-based works like Ref-Diff [7] attempt to use explicit land cover change priors to guide fusion, their reliance on additional change detection annotations limits their practical applicability. In contrast, our DS-DiT framework explores effective reference utilization without requiring any external change detection priors.

2.2 Conditional Diffusion Models for Super-Resolution

In recent years, diffusion models have achieved remarkable progress in image super-resolution owing to their powerful generative priors. SR3 [28] conditions on the LR image and performs super-resolution through iterative refinement. StableSR [34] leverages the generative prior of a pretrained text-to-image diffusion model for blind super-resolution. DiffBIR [21] adopts a two-stage strategy that first removes degradations and then supplements fine details via a diffusion model. PASD [41] introduces pixel-aware cross-attention, enabling the diffusion model to better perceive image structures. SeeSR [37] employs a degradation-aware prompt extractor to generate more realistic image details while preserving semantic consistency. DiT4SR [9] explores the capability of DiT-based diffusion models for real-world image super-resolution.

Despite their generative capability, diffusion models suffer from an inherent hallucination problem in SISR due to the lack of additional reference information, frequently producing textures inconsistent with the actual scene. Recent studies therefore combine RefSR with diffusion models, aiming to suppress hallucinations by leveraging Ref image information while generating high-quality images. CoSeR [31] uses a diffusion model to synthesize a corresponding reference image for the LR input, and then injects both into the denoising process via ControlNet. ReFIR [11] proposes a retrieval-augmented image restoration framework that exploits retrieved reference images to generate details faithful to the original scene. CRefDiff [32] fuses local and global information from the Ref image and leverages the generative prior of a diffusion model for real-world remote sensing image super-resolution. Ada-RefSR [36] follows a trust but verify principle, adaptively exploiting reliable reference information while suppressing unreliable parts.

2.3 Classifier-Free Guidance

Classifier-Free Guidance (CFG) [14] is a widely used inference-time technique for improving generation quality by extrapolating between conditional and unconditional predictions. Applying CFG typically requires jointly training models by dropping conditions with a fixed probability. However, in our framework, the text branch has been removed, and simply replacing the Ref image with an unrelated image to simulate unconditional generation can degrade reference utilization during normal inference. To circumvent the need for separate unconditional training, techniques like ICG [27] approximate unconditional predictions by sampling random independent conditions. Furthermore, Karras *et al.* [18] suggest using a smaller or under-trained version of the model in place of the unconditional model for guidance. Inspired by these self-guidance strategies, we propose an autoguidance strategy specifically tailored for the decoupled siamese DiT architecture. This strategy leverages the prediction discrepancy between strong and weak reference conditions to explicitly amplify reference utilization without additional training.

3 Methodology

In this work, we adopt conditional flow matching as the training paradigm to improve the reconstruction quality of RefSR at large scaling factors. The overall workflow of the proposed method is shown in Fig. 1. We modify the MM-DiT architecture and design a decoupled siamese diffusion transformer, which introduces LR and Ref images as conditioning modalities on equal footing. In the joint attention mechanism, the guidance from the LR and Ref branches is explicitly decoupled to prevent direct interaction between them, thereby alleviating inter-source competition. Furthermore, to capture local information that is easily overlooked by global attention, we adaptively fuse LR and Ref information at the patch level and inject the fused features into the denoising branch. During inference, we exploit the prediction discrepancy of the same model under different reference conditioning strengths to guide the denoising direction, further improving reconstruction quality without any additional training.

3.1 Preliminary

Unlike early diffusion models [13, 29] that rely on stochastic differential equations (SDEs) to describe the diffusion process, Flow Matching [22] directly models sample trajectories using ordinary differential equations (ODEs), resulting in more efficient training and faster sampling. Rectified Flow [23] further simplifies this modeling process by constraining the transport paths between samples to linear interpolation trajectories:

$$\mathbf{x}_t = (1 - t) \mathbf{x}_0 + t \mathbf{x}_1, \quad t \in [0, 1]. \quad (1)$$

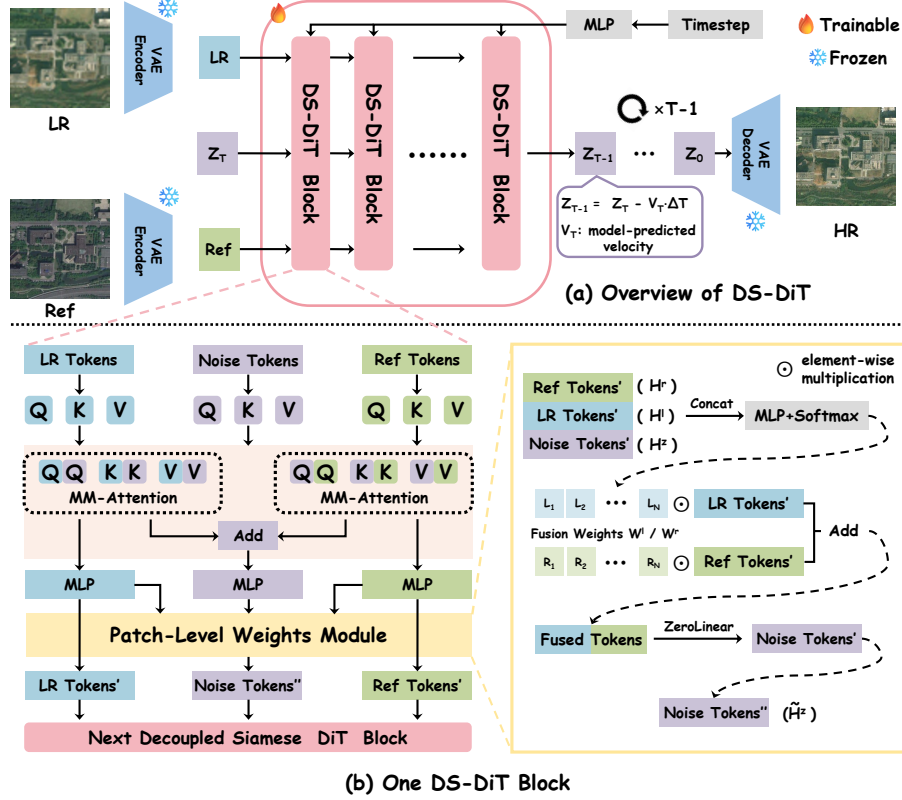


Fig. 1: Overall architecture of the proposed Decoupled Siamese Diffusion Transformer (DS-DiT). Our framework features a decoupled siamese interaction with a shared-QKV set to mitigate inter-source competition, complemented by a Patch-Level Weights (PLW) module for adaptive local feature fusion.

The training objective is to let the model-predicted velocity field \mathbf{v}_t^θ fit the ground-truth velocity field $\mathbf{v} = d\mathbf{x}_t/dt = \mathbf{x}_1 - \mathbf{x}_0$:

$$\mathcal{L}_{\text{RF}}(\theta) = \mathbb{E}_{t, \mathbf{x}_0, \mathbf{x}_1} \|\mathbf{v}_t^\theta - (\mathbf{x}_1 - \mathbf{x}_0)\|_2^2. \quad (2)$$

Current mainstream text-to-image models [2, 10, 30] adopt the MM-DiT architecture to predict the velocity field. Previous diffusion models typically rely on cross-attention to fuse image and text information, whereas MM-DiT designs independent Transformer branches for each modality. After encoding image and text features in their respective feature spaces, MM-DiT concatenates the resulting tokens along the sequence dimension and performs joint self-attention. This design enables image and text features to interact fully within a unified representation space, yielding superior multimodal fusion. Inspired by this, we treat the LR and Ref images as conditioning modalities and model them in the

same manner as the text modality in MM-DiT, enabling the model to fully exploit the structural information from the LR image and the texture information from the Ref image to reconstruct high-quality images.

3.2 Decoupling LR and Ref Interaction in MM-Attention

The text modality is unable to accurately describe land cover features in low-resolution remote sensing images, making it ineffective for RS super-resolution tasks. We therefore completely discard the text branch and model LR and Ref as new conditioning modalities. A straightforward idea is to construct an M³-DiT architecture that allows unconstrained interaction among all three modalities in the attention mechanism. Details of M³-DiT are provided in Sec. A of the appendix. However, in this setting, the softmax operation in self-attention forces information from different sources to compete for limited attention weights within a single unified sequence, leading to feature dilution where structural or texture priors are under-utilized. To alleviate this issue, we adopt a decoupled siamese architecture that decouples the interaction between the LR and Ref.

In CreatiLayout [45], the image branch generates independent sets of queries (Q), keys (K), and values (V) for the joint attention with each modality. In contrast, in our design, the noisy image tokens \mathbf{h}^z produce only a single set of Q, K, and V in each block, which is shared by both the LR and Ref branches. The interaction between LR and the noisy image is realized through MM-Attention:

$$\mathbf{h}_l^z, \mathbf{h}_{\text{new}}^l = \text{Attention}([\mathbf{h}^z \mathbf{W}_q^z, \mathbf{h}^l \mathbf{W}_q^l], [\mathbf{h}^z \mathbf{W}_k^z, \mathbf{h}^l \mathbf{W}_k^l], [\mathbf{h}^z \mathbf{W}_v^z, \mathbf{h}^l \mathbf{W}_v^l]), \quad (3)$$

where $[\cdot, \cdot]$ denotes concatenation along the sequence dimension, $\mathbf{W}_q^z, \mathbf{W}_k^z, \mathbf{W}_v^z$ are the learnable projection matrices for the noisy image branch, $\mathbf{W}_q^l, \mathbf{W}_k^l, \mathbf{W}_v^l$ are the corresponding projection matrices for the LR branch, and \mathbf{h}_l^z and $\mathbf{h}_{\text{new}}^l$ are the updated noisy image tokens and LR tokens after interaction, respectively. Meanwhile, Ref and the noisy image undergo the same joint attention mechanism:

$$\mathbf{h}_r^z, \mathbf{h}_{\text{new}}^r = \text{Attention}([\mathbf{h}^z \mathbf{W}_q^z, \mathbf{h}^r \mathbf{W}_q^r], [\mathbf{h}^z \mathbf{W}_k^z, \mathbf{h}^r \mathbf{W}_k^r], [\mathbf{h}^z \mathbf{W}_v^z, \mathbf{h}^r \mathbf{W}_v^r]). \quad (4)$$

The updated noisy image tokens are then obtained via a summation operation:

$$\mathbf{h}_{\text{new}}^z = \mathbf{h}_l^z + \mathbf{h}_r^z. \quad (5)$$

In this way, the guidance from LR and Ref is explicitly decoupled at the attention stage: each interacts with the noisy image independently, effectively mitigating inter-source competition.

3.3 Injecting LR and Ref Information via Patch-Level Weights

In the DiT architecture, the attention mechanism operates at the global level. However, relying solely on global attention may lead to the loss of local information [9], which is equally critical for recovering fine-grained image details. It is

therefore necessary to strengthen the fusion of LR and Ref features at the local level. Notably, the information provided by Ref is not entirely reliable, as land cover in certain regions may have changed between the acquisition times of LR and Ref. For such changed regions, the guidance from LR should be strengthened to maintain fidelity, whereas for regions where land cover remains unchanged, enhancing the guidance from Ref is more beneficial for recovering fine textures. Based on this analysis, we adaptively fuse LR and Ref through Patch-Level Weights and inject the fused features into the denoising branch.

Specifically, after the joint attention computation, the LR, Ref, and noisy image tokens $\mathbf{h}_{\text{new}}^l$, $\mathbf{h}_{\text{new}}^r$, and $\mathbf{h}_{\text{new}}^z$ are each passed through their respective MLPs, yielding feature tokens $\mathbf{H}^l, \mathbf{H}^r, \mathbf{H}^z \in \mathbb{R}^{N \times C}$. We first concatenate these three along the feature dimension and feed the result into a three-layer MLP, which outputs a per-patch weight map $\mathbf{W} \in \mathbb{R}^{N \times 2}$. A softmax operation is applied along the last dimension of \mathbf{W} to assign specific fusion weights for each patch, and the resulting weight map is then split into LR and Ref weights. The weighted LR and Ref features are then fused and injected into the noisy tokens as follows:

$$\tilde{\mathbf{H}}^z = \mathbf{H}^z + \text{ZeroLinear}(\mathbf{W}^l \odot \mathbf{H}^l + \mathbf{W}^r \odot \mathbf{H}^r), \quad (6)$$

where \mathbf{W}^l and \mathbf{W}^r are the per-patch weights for LR and Ref, respectively, ZeroLinear denotes a linear projection layer with zero-initialized weights to ensure training stability, \odot denotes element-wise multiplication with broadcasting, and $\tilde{\mathbf{H}}^z$ is the final output of the denoising branch in the current block.

3.4 Improving Image Quality with Autoguidance

In Conditional Rectified Flow, the ideal velocity field $\mathbf{v} = \mathbf{x}_1 - \mathbf{x}_0$ is a constant that depends only on the initial noise \mathbf{x}_1 and the target data \mathbf{x}_0 . In the RefSR task, however, given LR and Ref as two conditions, the model-predicted velocity field $\mathbf{v}_t^\theta(\mathbf{x}_t | c_{\text{lr}}, c_{\text{ref}})$ deviates from the ideal velocity field and varies with the current state \mathbf{x}_t . If the predicted velocity field can be corrected through guidance at each sampling step, the entire sampling trajectory can be optimized toward the target distribution, leading to higher-quality reconstruction.

In our siamese attention mechanism, the noisy image tokens are updated via $\mathbf{h}_{\text{new}}^z = \mathbf{h}_l^z + \mathbf{h}_r^z$. During sampling, we introduce a scaling coefficient λ for the tokens produced by the reference interaction path:

$$\mathbf{h}_{\text{new}}^z = \mathbf{h}_l^z + \lambda \mathbf{h}_r^z. \quad (7)$$

When $\lambda = 1$, the model predicts the velocity field $\mathbf{v}_t^\theta(\mathbf{x}_t | c_{\text{lr}}, c_{\text{ref}})$ in its original direction. To construct a weak reference condition, we set $\lambda = 0$, which eliminates the direct contribution of the Ref branch to the noisy tokens and significantly reduces the guidance strength. The model then predicts a weakened velocity field $\mathbf{v}_t^{\theta^-}(\mathbf{x}_t | c_{\text{lr}}, c_{\text{ref}}^-)$. Analogous to the extrapolation form of CFG, the corrected velocity field $\mathbf{v}_t^{\theta^+}$ can be expressed as:

$$\mathbf{v}_t^{\theta^+}(\mathbf{x}_t | c_{\text{lr}}, c_{\text{ref}}^+) = (1 - \omega) \mathbf{v}_t^{\theta^-}(\mathbf{x}_t | c_{\text{lr}}, c_{\text{ref}}^-) + \omega \mathbf{v}_t^\theta(\mathbf{x}_t | c_{\text{lr}}, c_{\text{ref}}), \quad (8)$$

where ω is the guidance coefficient. When $\omega > 1$, the prediction trajectory is extrapolated along the reference guidance direction, shifting toward more thorough exploitation of the texture information from Ref. It should be noted that, to preserve the structural fidelity of the reconstructed image, ω must be kept within a moderate range to prevent the prediction from departing from the structural constraints imposed by the LR image. A detailed analysis of the influence of ω is provided in the appendix.

4 Experiments

4.1 Experimental Settings

Datasets. SECOND [40] is a semantic change detection dataset comprising 4,662 pairs of aerial images. Each image has a size of 512×512 pixels with a spatial resolution ranging from 0.5 to 3 meters. The dataset covers six major land cover categories across diverse sensors and regions, encompassing various imaging styles and scene types. We follow the official split [40], using 2,968 image pairs for training and 1,694 pairs for testing. FUSU [44] is a high-resolution aerial land cover change detection dataset sourced from Google Earth, annotated with 17 land cover categories. The cropped images are 512×512 in size with a spatial resolution of 0.2 to 0.5 meters. We select 7,436 image pairs for training and 2,192 pairs for testing.

Implementation Details. We conduct super-resolution experiments at two challenging scaling factors: $\times 8$ and $\times 16$. Low-resolution (LR) images are generated via bicubic downsampling. While we do not simulate complex real-world degradations, these large scaling factors themselves pose significant challenges for structural and textural recovery. DS-DiT is built upon the pretrained MM-DiT blocks of SD3 [10]. Specifically, we extract the denoising branch weights to initialize the dual siamese branches to provide a strong generative prior. The model is trained at a resolution of 512×512 , with LR images upsampled to this size using bicubic interpolation before input. We utilize the AdamW [24] optimizer with a learning rate of 5×10^{-5} and a weight decay of 0.001. Training is performed on four NVIDIA A100 GPUs with a total batch size of 16 for 80k steps, taking approximately 21 hours. For inference, we use the Euler ODE solver with 40 steps. The guidance coefficient ω is set to 1.2 for the SECOND dataset and 1.1 for the FUSU dataset.

Evaluation Metrics. To quantitatively evaluate RefSR performance, we adopt three reference-based perceptual metrics. LPIPS [48] measures perceptual similarity between images using features extracted by a pretrained deep network. FID [12] computes the distributional distance between generated and real images in feature space. DISTS [5] evaluates structural and textural similarity. Compared to PSNR and SSIM, these metrics are more suitable for assessing generative super-resolution methods [41]. In addition, we introduce two no-reference metrics, CLIPQA [33] and MUSIQ [19], to comprehensively evaluate the visual quality of reconstructed images.

Table 1: Quantitative comparison of RefSR methods on the SECOND and FUSU datasets at $\times 8$ and $\times 16$ scaling factors. **Red** indicates the best and **blue** indicates the second-best result. The metrics are evaluated on the full test sets.

Dataset	Scale	Metric	TTSR	DATSR	CoSeR*	Ref-Diff	CreatiLayout*	M ³ -DiT	Ours
SECOND	$\times 8$	LPIPS \downarrow	0.2994	0.3835	0.2576	0.2819	0.2692	0.2417	0.2174
		FID \downarrow	34.62	40.87	23.06	28.48	24.05	22.66	15.87
		DISTS \downarrow	0.1518	0.1923	0.1289	0.1490	0.1412	0.1356	0.1090
		CLIPQA \uparrow	0.2937	0.2076	0.2973	0.4361	0.4255	0.4434	0.4698
		MUSIQ \uparrow	43.86	27.36	42.11	51.36	43.18	44.92	49.04
	$\times 16$	LPIPS \downarrow	0.3927	0.5039	0.3426	0.3503	0.3556	0.3504	0.2905
		FID \downarrow	134.68	99.74	31.12	30.11	32.03	35.50	21.58
		DISTS \downarrow	0.2196	0.2555	0.1595	0.1555	0.1670	0.1715	0.1334
		CLIPQA \uparrow	0.3391	0.1554	0.3134	0.3468	0.4530	0.4489	0.4875
		MUSIQ \uparrow	37.71	22.02	42.18	49.75	43.55	43.65	48.65
FUSU	$\times 8$	LPIPS \downarrow	0.2960	0.3295	0.2447	0.2809	0.2143	0.2167	0.1741
		FID \downarrow	54.73	35.06	24.69	26.21	16.88	17.95	13.01
		DISTS \downarrow	0.1660	0.1803	0.1346	0.1618	0.1282	0.1289	0.1054
		CLIPQA \uparrow	0.4998	0.2623	0.4178	0.5495	0.5076	0.5095	0.5306
		MUSIQ \uparrow	51.33	32.82	49.54	54.43	51.45	51.45	52.84
	$\times 16$	LPIPS \downarrow	0.3398	0.4546	0.2954	0.3288	0.2766	0.2641	0.2301
		FID \downarrow	127.12	104.78	35.01	34.26	20.55	20.35	19.52
		DISTS \downarrow	0.1949	0.2493	0.1652	0.1714	0.1510	0.1456	0.1309
		CLIPQA \uparrow	0.4836	0.2360	0.4036	0.5175	0.5066	0.5101	0.5339
		MUSIQ \uparrow	48.85	27.72	49.11	53.00	50.78	51.55	53.21

4.2 Comparison with Existing Methods

We compare the proposed method with state-of-the-art GAN-based and diffusion-based RefSR methods. These include two GAN-based methods (TTSR [39] and DATSR [3]), two UNet-based diffusion methods (CoSeR* [31] and Ref-Diff [7]), and two DiT-based methods (CreatiLayout* [45] and M³-DiT introduced in Sec. 3.2). Specifically, CoSeR* denotes an adapted version of the original method, in which the automatically generated reference image is replaced with the paired real reference image from the dataset. CreatiLayout* is likewise adapted for the RefSR task by replacing the original text and layout inputs with LR and Ref, and adopting a two-stage training strategy: a SISR model is first trained, after which most parameters are frozen and the Ref branch is introduced for continued training.

Quantitative Comparison. Tab. 1 presents the quantitative comparison results on two datasets at two large scaling factors ($\times 8$ and $\times 16$). Across all four experimental settings, the proposed method achieves the best performance on all reference-based metrics and significantly outperforms the second-best method, demonstrating that our results possess both high fidelity and perceptual quality. On the no-reference metrics, our method also shows strong competitiveness, falling slightly behind Ref-Diff only in certain settings. As shown in Fig. 2, Ref-Diff tends to generate visually rich yet less faithful textures in some regions. Since no-reference metrics such as CLIPQA [33] and MUSIQ [19] primarily re-

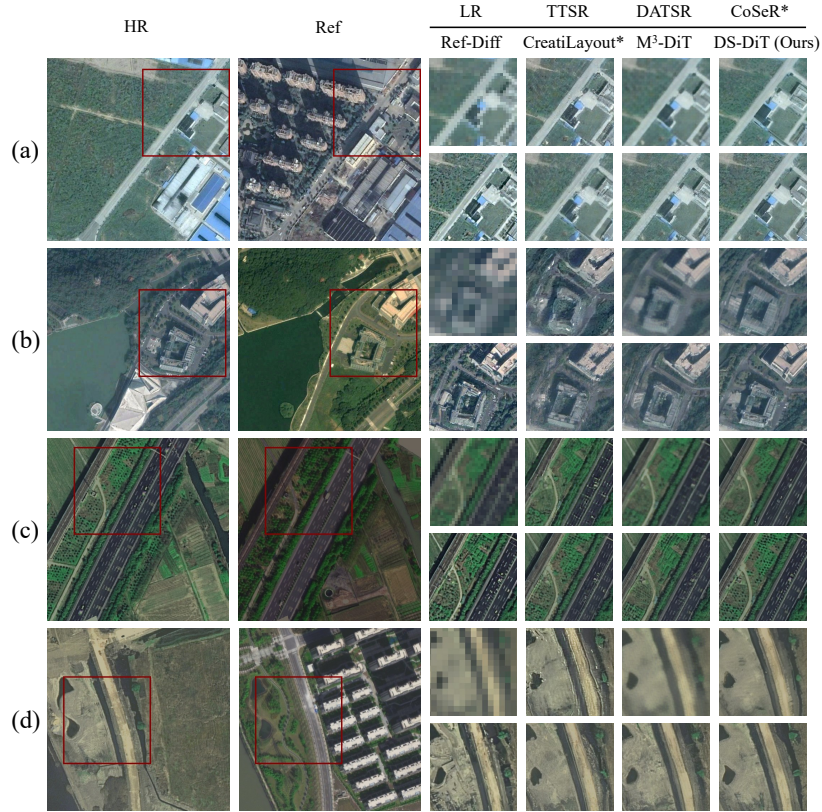


Fig. 2: Qualitative comparison of different RefSR methods on the SECOND and FUSU datasets. The visual results correspond to: (a) SECOND at $\times 8$ scaling factor, (b) SECOND at $\times 16$ scaling factor, (c) FUSU at $\times 8$ scaling factor, and (d) FUSU at $\times 16$ scaling factor.

flect perceptual quality rather than explicit fidelity to the ground truth, such rich but non-authentic details may still receive higher scores. In contrast, our method achieves a better balance between reconstruction fidelity and perceptual realism.

Qualitative Comparison. Fig. 2 provides visual comparison results. Fig. 2(a) shows an example from the SECOND $\times 8$ dataset with substantial land cover changes. Even though only a few regions remain unchanged, our method successfully extracts the corresponding textures and reconstructs the fine details of the buildings on the right side of the image. Fig. 2(b) presents an example from the SECOND $\times 16$ dataset with minor changes. At this extreme scaling factor, other methods fail to transfer textures successfully, producing artifacts or blurry results despite the valuable information provided by Ref. In contrast, our method captures usable texture information and transfers it effectively, recovering the

complex structures of the buildings. Fig. 2(c) illustrates an example from the FUSU $\times 8$ dataset. When the vegetation information in Ref is untrustworthy due to seasonal changes, our method avoids blindly transferring erroneous textures; meanwhile, it effectively exploits reliable road textures to assist reconstruction—a selective transfer capability that other methods lack. Finally, Fig. 2(d) shows an example from the FUSU $\times 16$ dataset with drastic changes, where our method still successfully recovers the clear shapes of the lake and the river. In summary, the qualitative comparisons further validate the effectiveness of the proposed method, which selectively exploits Ref information rather than blindly copying it. Under the structural constraints imposed by LR, our approach generates reconstructed results with higher fidelity and superior perceptual quality.

4.3 Ablation Study

We conduct ablation studies on the SECOND dataset at both $\times 8$ and $\times 16$ scaling factors to validate the effectiveness of each component. Detailed results are presented in Tab. 2.

Importance of Decoupled Siamese Attention. Compared to M^3 -Attention, our decoupled siamese attention segregates the interaction between LR and Ref images. Although this avoids their explicit interaction within the same attention layer, it achieves superior performance on nearly all metrics (see the comparison between M^3 -DiT in Tab. 1 and the siamese attention baseline in Tab. 2). This confirms that by mitigating inter-source competition, the decoupled architecture improves information utilization and prevents feature dilution. As observed in Fig. 3(a) and Fig. 3(b), this architecture recovers more building and ground details compared to M^3 -Attention.

Effect of Patch-Level Weights Module. After introducing the PLW module, all three reference-based metrics show consistent improvement, indicating that this module effectively compensates for the deficiency of global attention in local modeling. By adaptively modulating the fusion weights based on the local context, the PLW module suppresses artifacts in changed regions while enhancing textures in unchanged areas. Fig. 3(c) further corroborates this observation, as the texture details of buildings are noticeably sharper and more refined.

Effect of Autoguidance. When autoguidance is applied to the baseline model, all metrics are improved, with particularly significant gains in perceptual and no-reference metrics. This indicates that the corrected velocity field steers the sampling trajectory toward data distributions with richer high-frequency details, thereby producing more realistic reconstructions.

Complementarity of Components. When both modules are introduced simultaneously, all metrics reach their optimal values, with improvements exceeding the simple summation of gains from introducing either module individually, demonstrating strong complementarity between the two. LR and Ref injection focuses on accurate recovery of local structures, while autoguidance enhances global textural realism; their synergy drives a comprehensive improvement in reconstruction quality. The reconstruction in Fig. 3(d) maintains high fidelity while exhibiting stronger perceptual realism.

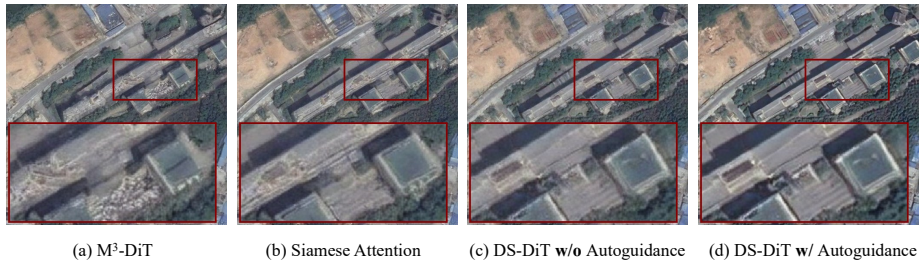


Fig. 3: Visual ablation study on the SECOND dataset ($\times 16$ scaling factor).

Table 2: Ablation study on the SECOND dataset. The results are reported for $\times 8$ (upper four rows) and $\times 16$ (lower four rows) scaling factors. \checkmark indicates the component is included. The best result in each group is highlighted in **bold**.

Siamese Attention	PLW Module	Auto-guidance	LPIPS \downarrow	FID \downarrow	DISTS \downarrow	CLIPQA \uparrow	MUSIQ \uparrow
\checkmark			0.2362	19.16	0.1251	0.4403	44.95
\checkmark	\checkmark		0.2291	18.93	0.1234	0.4399	45.07
\checkmark		\checkmark	0.2278	18.56	0.1159	0.4680	48.29
\checkmark	\checkmark	\checkmark	0.2174	15.87	0.1090	0.4698	49.04
\checkmark			0.3159	31.29	0.1571	0.4514	43.78
\checkmark	\checkmark		0.3085	30.32	0.1557	0.4604	43.88
\checkmark		\checkmark	0.3060	27.96	0.1449	0.4649	46.60
\checkmark	\checkmark	\checkmark	0.2905	21.58	0.1334	0.4875	48.65

4.4 Discussion on LR and Ref Injection Strategy

It is worth noting that not all injection strategies lead to performance improvements. We initially designed two simpler injection approaches. Variant A keeps LR and Ref isolated from each other, avoiding their explicit interaction. The LR tokens \mathbf{H}^l and Ref tokens \mathbf{H}^r are injected into the noisy tokens \mathbf{H}^z through independent zero-initialized linear layers:

$$\tilde{\mathbf{H}}^z = \mathbf{H}^z + \text{ZeroLinear}(\mathbf{H}^l) + \text{ZeroLinear}(\mathbf{H}^r). \quad (9)$$

Variant B directly sums LR and Ref before injecting them into the noisy tokens through a single zero-initialized linear layer:

$$\tilde{\mathbf{H}}^z = \mathbf{H}^z + \text{ZeroLinear}(\mathbf{H}^l + \mathbf{H}^r). \quad (10)$$

Our proposed Patch-Level Weights (PLW) injection strategy is denoted as Variant C, with the corresponding formulation given in Eq. (6). The comparison results on the SECOND $\times 8$ dataset are presented in Tab. 3.

Variant A improves PSNR and SSIM but yields a higher FID, indicating that independent injection can provide some structural information yet lacks

Table 3: Comparison of different injection strategies on the SECOND $\times 8$ dataset. The best result is highlighted in **bold**.

Method	PSNR \uparrow	SSIM \uparrow	LPIPS \downarrow	FID \downarrow	DISTS \downarrow
Siamese Attention	24.50	0.5921	0.2362	19.16	0.1251
+ Variant A	24.63	0.5981	0.2327	23.07	0.1303
+ Variant B	24.63	0.5966	0.2308	19.81	0.1254
+ Variant C (PLW)	24.70	0.6005	0.2291	18.93	0.1234

the ability to distinguish the reliability of LR and Ref information. Variant B fuses the two sources by direct summation, achieving a lower FID than Variant A but still falling short of the baseline, suggesting that naive equal-weight fusion neglects the varying reliability of LR and Ref across different regions. In contrast, Variant C (PLW) outperforms the baseline on all metrics, owing to its per-patch adaptive weight allocation mechanism.

However, the design of the PLW module implicitly assumes that LR and Ref are roughly spatially aligned. This assumption generally holds in remote sensing scenarios, where both images originate from the same geographic location. For spatially misaligned reference images, *e.g.*, captured from different viewpoints or covering different regions, the per-patch weight allocation would lose its spatial correspondence, potentially leading to degraded performance. How to adaptively retrieve and exploit useful texture information from spatially misaligned reference images remains an important direction for our future exploration.

5 Conclusion

In this work, we propose the Decoupled Siamese Diffusion Transformer (DS-DiT), a framework designed to balance LR structural fidelity and Ref texture utilization in RS RefSR. By introducing the decoupled siamese attention mechanism, our model effectively separates structural and textural interactions, ensuring that the noisy latent remains anchored to the original geometric layout while incorporating high-frequency details. To further address the challenges of land cover changes and the limitations of global attention, we design a Patch-Level Weights module to adaptively modulate feature fusion at the local level. Additionally, we introduce an autoguidance strategy that boosts reconstruction quality during inference by exploiting the model’s internal structural priors without requiring additional training. This work demonstrates the significant potential of decoupled diffusion transformers for high-fidelity remote sensing reconstruction, providing a robust and flexible paradigm for practical applications where precise texture recovery must be balanced with strict structural authenticity.

Acknowledgement

This research was supported in part by the National Natural Science Foundation of China (Grant No. T2125006) and the Natural Science Foundation of Guangdong Province, China (Grant No. 2026A1515010676).

References

1. Ahn, D., Cho, H., Min, J., Jang, W., Kim, J., Kim, S., Park, H.H., Jin, K.H., Kim, S.: Self-rectifying diffusion sampling with perturbed-attention guidance. In: European Conference on Computer Vision. pp. 1–17. Springer (2024)
2. Black Forest Labs: Flux. <https://blackforestlabs.ai/announcing-black-forest-labs> (2024)
3. Cao, J., Liang, J., Zhang, K., Li, Y., Zhang, Y., Wang, W., Gool, L.V.: Reference-based image super-resolution with deformable attention transformer. In: European conference on computer vision. pp. 325–342. Springer (2022)
4. Chen, J., Pan, J., Dong, J.: Faithdiff: Unleashing diffusion priors for faithful image super-resolution. In: Proceedings of the Computer Vision and Pattern Recognition Conference. pp. 28188–28197 (2025)
5. Ding, K., Ma, K., Wang, S., Simoncelli, E.P.: Image quality assessment: Unifying structure and texture similarity. *IEEE transactions on pattern analysis and machine intelligence* **44**(5), 2567–2581 (2020)
6. Dong, R., Mou, L., Chen, M., Li, W., Tong, X.Y., Yuan, S., Zhang, L., Zheng, J., Zhu, X., Fu, H.: Large-scale land cover mapping with fine-grained classes via class-aware semi-supervised semantic segmentation. In: Proceedings of the IEEE/CVF International Conference on Computer Vision. pp. 16783–16793 (2023)
7. Dong, R., Yuan, S., Luo, B., Chen, M., Zhang, J., Zhang, L., Li, W., Zheng, J., Fu, H.: Building bridges across spatial and temporal resolutions: Reference-based super-resolution via change priors and conditional diffusion model. In: Proceedings of the IEEE/CVF Conference on Computer Vision and Pattern Recognition (CVPR). pp. 27684–27694 (June 2024)
8. Dong, R., Zhang, L., Fu, H.: Rrsgan: Reference-based super-resolution for remote sensing image. *IEEE Transactions on Geoscience and Remote Sensing* **60**, 1–17 (2021)
9. Duan, Z.P., Zhang, J., Jin, X., Zhang, Z., Xiong, Z., Zou, D., Ren, J.S., Guo, C., Li, C.: Dit4sr: Taming diffusion transformer for real-world image super-resolution. In: Proceedings of the IEEE/CVF International Conference on Computer Vision (ICCV). pp. 18948–18958 (October 2025)
10. Esser, P., Kulal, S., Blattmann, A., Entezari, R., Müller, J., Saini, H., Levi, Y., Lorenz, D., Sauer, A., Boesel, F., et al.: Scaling rectified flow transformers for high-resolution image synthesis. In: Forty-first international conference on machine learning (2024)
11. Guo, H., Dai, T., Ouyang, Z., Zhang, T., Zha, Y., Chen, B., Xia, S.t.: Refir: Grounding large restoration models with retrieval augmentation. *Advances in Neural Information Processing Systems* **37**, 46593–46621 (2024)
12. Heusel, M., Ramsauer, H., Unterthiner, T., Nessler, B., Hochreiter, S.: Gans trained by a two time-scale update rule converge to a local nash equilibrium. *Advances in neural information processing systems* **30** (2017)

13. Ho, J., Jain, A., Abbeel, P.: Denoising diffusion probabilistic models. *Advances in neural information processing systems* **33**, 6840–6851 (2020)
14. Ho, J., Salimans, T.: Classifier-free diffusion guidance. *arXiv preprint arXiv:2207.12598* (2022)
15. Hong, S.: Smoothed energy guidance: Guiding diffusion models with reduced energy curvature of attention. *Advances in Neural Information Processing Systems* **37**, 66743–66772 (2024)
16. Jiang, J., Zhang, Q., Yao, X., Tian, Y., Zhu, Y., Cao, W., Cheng, T.: Histif: A new spatiotemporal image fusion method for high-resolution monitoring of crops at the subfield level. *IEEE Journal of Selected Topics in Applied Earth Observations and Remote Sensing* **13**, 4607–4626 (2020)
17. Jiang, Y., Chan, K.C., Wang, X., Loy, C.C., Liu, Z.: Robust reference-based super-resolution via c2-matching. In: *Proceedings of the IEEE/CVF Conference on Computer Vision and Pattern Recognition*. pp. 2103–2112 (2021)
18. Karras, T., Aittala, M., Kynkäänniemi, T., Lehtinen, J., Aila, T., Laine, S.: Guiding a diffusion model with a bad version of itself. *Advances in Neural Information Processing Systems* **37**, 52996–53021 (2024)
19. Ke, J., Wang, Q., Wang, Y., Milanfar, P., Yang, F.: Musiq: Multi-scale image quality transformer. In: *Proceedings of the IEEE/CVF International Conference on Computer Vision*. pp. 5148–5157 (2021)
20. Labs, B.F., Batifol, S., Blattmann, A., Boesel, F., Consul, S., Diagne, C., Dockhorn, T., English, J., English, Z., Esser, P., et al.: Flux. 1 kontekst: Flow matching for in-context image generation and editing in latent space. *arXiv preprint arXiv:2506.15742* (2025)
21. Lin, X., He, J., Chen, Z., Lyu, Z., Dai, B., Yu, F., Qiao, Y., Ouyang, W., Dong, C.: Diffbir: Toward blind image restoration with generative diffusion prior. In: *European conference on computer vision*. pp. 430–448. Springer (2024)
22. Lipman, Y., Chen, R.T., Ben-Hamu, H., Nickel, M., Le, M.: Flow matching for generative modeling. *arXiv preprint arXiv:2210.02747* (2022)
23. Liu, X., Gong, C., Liu, Q.: Flow straight and fast: Learning to generate and transfer data with rectified flow. *arXiv preprint arXiv:2209.03003* (2022)
24. Loshchilov, I., Hutter, F.: Decoupled weight decay regularization. *arXiv preprint arXiv:1711.05101* (2017)
25. Lu, L., Li, W., Tao, X., Lu, J., Jia, J.: Masa-sr: Matching acceleration and spatial adaptation for reference-based image super-resolution. In: *Proceedings of the IEEE/CVF Conference on Computer Vision and Pattern Recognition*. pp. 6368–6377 (2021)
26. Rombach, R., Blattmann, A., Lorenz, D., Esser, P., Ommer, B.: High-resolution image synthesis with latent diffusion models. In: *Proceedings of the IEEE/CVF conference on computer vision and pattern recognition*. pp. 10684–10695 (2022)
27. Sadat, S., Kansy, M., Hilliges, O., Weber, R.: No training, no problem: Rethinking classifier-free guidance for diffusion models. In: *International Conference on Learning Representations*. vol. 2025, pp. 76833–76858 (2025)
28. Saharia, C., Ho, J., Chan, W., Salimans, T., Fleet, D.J., Norouzi, M.: Image super-resolution via iterative refinement. *IEEE transactions on pattern analysis and machine intelligence* **45**(4), 4713–4726 (2022)
29. Song, J., Meng, C., Ermon, S.: Denoising diffusion implicit models. *arXiv preprint arXiv:2010.02502* (2020)
30. Stability AI: Stable diffusion 3.5. <https://stability.ai/news/introducing-stable-diffusion-3-5> (2024)

31. Sun, H., Li, W., Liu, J., Chen, H., Pei, R., Zou, X., Yan, Y., Yang, Y.: Coser: Bridging image and language for cognitive super-resolution. In: Proceedings of the IEEE/CVF Conference on Computer Vision and Pattern Recognition (CVPR). pp. 25868–25878 (June 2024)
32. Wang, C., Sun, W.: Controllable reference-guided diffusion with local-global fusion for real-world remote sensing super-resolution. *IEEE Journal of Selected Topics in Applied Earth Observations and Remote Sensing* (2026)
33. Wang, J., Chan, K.C., Loy, C.C.: Exploring clip for assessing the look and feel of images. In: AAAI (2023)
34. Wang, J., Yue, Z., Zhou, S., Chan, K.C., Loy, C.C.: Exploiting diffusion prior for real-world image super-resolution. *International Journal of Computer Vision* **132**(12), 5929–5949 (2024)
35. Wang, X., Xie, L., Dong, C., Shan, Y.: Real-esrgan: Training real-world blind super-resolution with pure synthetic data. In: Proceedings of the IEEE/CVF international conference on computer vision. pp. 1905–1914 (2021)
36. Wang, Y., Wan, Y., Zheng, S., Li, B., Hou, Q., Jiang, P.T.: Trust but verify: Adaptive conditioning for reference-based diffusion super-resolution via implicit reference correlation modeling (2026), <https://arxiv.org/abs/2602.01864>
37. Wu, R., Yang, T., Sun, L., Zhang, Z., Li, S., Zhang, L.: Seesr: Towards semantics-aware real-world image super-resolution. In: Proceedings of the IEEE/CVF Conference on Computer Vision and Pattern Recognition (CVPR). pp. 25456–25467 (June 2024)
38. Xia, B., Tian, Y., Hang, Y., Yang, W., Liao, Q., Zhou, J.: Coarse-to-fine embedded patchmatch and multi-scale dynamic aggregation for reference-based super-resolution. In: Proceedings of the aai conference on artificial intelligence. vol. 36, pp. 2768–2776 (2022)
39. Yang, F., Yang, H., Fu, J., Lu, H., Guo, B.: Learning texture transformer network for image super-resolution. In: Proceedings of the IEEE/CVF conference on computer vision and pattern recognition. pp. 5791–5800 (2020)
40. Yang, K., Xia, G.S., Liu, Z., Du, B., Yang, W., Pelillo, M., Zhang, L.: Semantic change detection with asymmetric siamese networks. arXiv preprint arXiv:2010.05687 (2020)
41. Yang, T., Wu, R., Ren, P., Xie, X., Zhang, L.: Pixel-aware stable diffusion for realistic image super-resolution and personalized stylization. In: European conference on computer vision. pp. 74–91. Springer (2024)
42. Yang, Y., Zhang, Y., Zhang, K., Zhang, J., Chen, X., Fu, H., Dong, R.: Task-oriented data synthesis and control-rectify sampling for remote sensing semantic segmentation. arXiv preprint arXiv:2512.16740 (2025)
43. Yu, F., Gu, J., Li, Z., Hu, J., Kong, X., Wang, X., He, J., Qiao, Y., Dong, C.: Scaling up to excellence: Practicing model scaling for photo-realistic image restoration in the wild. In: Proceedings of the IEEE/CVF conference on computer vision and pattern recognition. pp. 25669–25680 (2024)
44. Yuan, S., Lin, G., Zhang, L., Dong, R., Zhang, J., Chen, S., Zheng, J., Wang, J., Fu, H.: Fusu: A multi-temporal-source land use change segmentation dataset for fine-grained urban semantic understanding. *Advances in Neural Information Processing Systems* **37**, 132417–132439 (2024)
45. Zhang, H., Hong, D., Wang, Y., Shao, J., Wu, X., Wu, Z., Jiang, Y.G.: Creatilayout: Siamese multimodal diffusion transformer for creative layout-to-image generation. In: Proceedings of the IEEE/CVF International Conference on Computer Vision (ICCV). pp. 18487–18497 (October 2025)

46. Zhang, J., Zhang, W., Jiang, B., Tong, X., Chai, K., Yin, Y., Wang, L., Jia, J., Chen, X.: Reference-based super-resolution method for remote sensing images with feature compression module. *Remote Sensing* **15**(4), 1103 (2023)
47. Zhang, L., Rao, A., Agrawala, M.: Adding conditional control to text-to-image diffusion models. In: *Proceedings of the IEEE/CVF international conference on computer vision*. pp. 3836–3847 (2023)
48. Zhang, R., Isola, P., Efros, A.A., Shechtman, E., Wang, O.: The unreasonable effectiveness of deep features as a perceptual metric. In: *Proceedings of the IEEE conference on computer vision and pattern recognition*. pp. 586–595 (2018)
49. Zhang, Y., Zhang, Z., DiVerdi, S., Wang, Z., Echevarria, J., Fu, Y.: Texture hallucination for large-factor painting super-resolution. In: *European Conference on Computer Vision*. pp. 209–225. Springer (2020)
50. Zhang, Z., Wang, Z., Lin, Z., Qi, H.: Image super-resolution by neural texture transfer. In: *Proceedings of the IEEE/CVF conference on computer vision and pattern recognition*. pp. 7982–7991 (2019)
51. Zheng, H., Ji, M., Wang, H., Liu, Y., Fang, L.: Crossnet: An end-to-end reference-based super resolution network using cross-scale warping. In: *Proceedings of the European Conference on Computer Vision (ECCV)* (September 2018)
52. Zhou, Y., Wang, J., Ding, J., Liu, B., Weng, N., Xiao, H.: Signet: A siamese graph convolutional network for multi-class urban change detection. *Remote Sensing* **15**(9), 2464 (2023)

Appendix

A Detailed Illustration of M³-DiT

As mentioned in Sec. 3.2, we adapt M³-DiT for RefSR and include it as a comparison method. Here we provide a more detailed description. As illustrated in Fig. 4, the noisy image tokens \mathbf{h}^z produce a set of query, key, and value matrices in each block: $\mathbf{Q}^z = \mathbf{h}^z \mathbf{W}_q^z$, $\mathbf{K}^z = \mathbf{h}^z \mathbf{W}_k^z$, $\mathbf{V}^z = \mathbf{h}^z \mathbf{W}_v^z$, where \mathbf{W}_q^z , \mathbf{W}_k^z , and \mathbf{W}_v^z are the weight matrices of the query, key, and value projection layers for \mathbf{h}^z . Likewise, the LR tokens \mathbf{h}^l and Ref tokens \mathbf{h}^r produce their respective queries, keys, and values: $\mathbf{Q}^l, \mathbf{K}^l, \mathbf{V}^l$ and $\mathbf{Q}^r, \mathbf{K}^r, \mathbf{V}^r$. The interaction among all three information sources is then realized through M³-Attention:

$$\mathbf{h}_{\text{new}}^z, \mathbf{h}_{\text{new}}^l, \mathbf{h}_{\text{new}}^r = \text{Attention}([\mathbf{Q}^z, \mathbf{Q}^l, \mathbf{Q}^r], [\mathbf{K}^z, \mathbf{K}^l, \mathbf{K}^r], [\mathbf{V}^z, \mathbf{V}^l, \mathbf{V}^r]), \quad (11)$$

where $[\cdot, \cdot, \cdot]$ denotes concatenation along the sequence dimension, and $\mathbf{h}_{\text{new}}^z$, $\mathbf{h}_{\text{new}}^l$, and $\mathbf{h}_{\text{new}}^r$ are the updated tokens after interaction. Unlike our siamese attention design, M³-DiT allows unconstrained interaction among all branches within a single unified attention sequence.

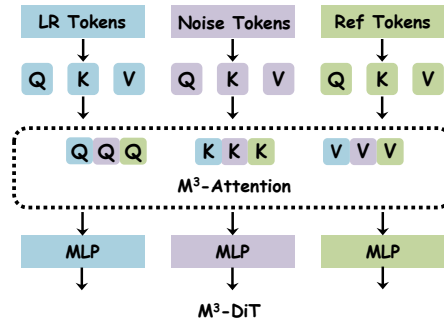


Fig. 4: The architecture of M³-DiT.

B Experiments on Additional Datasets

To further evaluate the generalization ability of our model, we conduct additional experiments on two datasets, i.e., CNAM-CD [52] and Real-RefRSSRD [32]. These experiments are intended to assess whether the proposed method can maintain its effectiveness under different data distributions and more realistic remote sensing degradation settings.

CNAM-CD. CNAM-CD [52] is a remote sensing change detection dataset collected from Google Earth, with a spatial resolution of 0.5 m. In our experiments, we use 1,758 image pairs for training and 750 image pairs for testing.

Table 4: Quantitative comparison on CNAM-CD and Real-RefRSSRD. Red indicates the best and blue indicates the second-best result. (Creati* denotes CreatiLayout*.)

Dataset	Scale	Metric	CoSeR*	Ref-Diff	Creati*	M ³ -DiT	Ours
CNAM-CD	×8	LPIPS ↓	0.2593	0.2787	0.2560	0.2566	0.2101
		FID ↓	51.00	51.97	45.92	46.50	35.76
		DISTS ↓	0.1365	0.1465	0.1434	0.1441	0.1109
		CLIPQA ↑	0.3322	0.3794	0.4058	0.3980	0.4446
		MUSIQ ↑	36.85	47.15	39.71	40.06	44.08
	×16	LPIPS ↓	0.3319	0.3405	0.3506	0.3486	0.2789
		FID ↓	62.99	60.76	72.05	64.84	45.79
		DISTS ↓	0.1716	0.1545	0.1915	0.1827	0.1361
		CLIPQA ↑	0.3301	0.3284	0.4019	0.4052	0.4325
		MUSIQ ↑	34.79	46.25	36.82	38.97	43.35
Real-RefRSSRD	×10	LPIPS ↓	0.4459	0.3979	0.3825	0.3756	0.3261
		FID ↓	52.33	48.20	34.64	35.18	31.56
		DISTS ↓	0.2450	0.2067	0.2192	0.2072	0.1809
		CLIPQA ↑	0.4818	0.5870	0.6281	0.6299	0.6456
		MUSIQ ↑	46.07	56.43	57.07	56.90	57.09

Real-RefRSSRD. We also evaluate our method on Real-RefRSSRD [32], a real-world remote sensing RefSR dataset. Unlike evaluation based on synthetic degradation, Real-RefRSSRD contains paired HR and LR satellite images collected from different sensors. Specifically, the HR images are from NAIP with a ground sampling distance of 1 m, while the LR images are from Sentinel-2 with a ground sampling distance of 10 m. This dataset reflects a more realistic scenario.

As shown in Tab. 4, our method achieves the best results on most metrics across CNAM-CD and Real-RefRSSRD. These results demonstrate the generalization ability of our model.

C Autoguidance Analysis

C.1 Effect of Guidance Coefficient ω

As described in Sec. 3.4, the noisy image tokens in the siamese attention are updated via $\mathbf{h}_{\text{new}}^z = \mathbf{h}_l^z + \lambda \mathbf{h}_r^z$. Autoguidance corrects the velocity field by extrapolating between the normal conditional prediction $\mathbf{v}_t^\theta(\mathbf{x}_t | c_{\text{lr}}, c_{\text{ref}})$ ($\lambda = 1$) and the weakened conditional prediction $\mathbf{v}_t^{\theta^-}(\mathbf{x}_t | c_{\text{lr}}, c_{\text{ref}}^-)$ ($\lambda = 0$), with the guidance coefficient ω controlling the extrapolation strength.

To systematically analyze the effect of ω on reconstruction quality, we evaluate $\omega \in \{0, 1.0, 1.1, 1.2, 1.3, 1.4, 1.5\}$ on the SECOND dataset at both ×8 and ×16 scaling factors. The complete results are presented in Tab. 5. When $\omega = 0$, the prediction direction reduces to $\mathbf{v}_t^{\theta^-}$, where the direct contribution of the

Table 5: Effect of the guidance coefficient ω on reconstruction quality on the SECOND dataset at $\times 8$ and $\times 16$ scaling factors.

Scale	ω	PSNR \uparrow	SSIM \uparrow	LPIPS \downarrow	FID \downarrow	DISTS \downarrow	CLIQQA \uparrow	MUSIQ \uparrow
$\times 8$	0	23.11	0.5408	0.4465	75.14	0.2947	0.2691	23.47
	1.0	24.70	0.6005	0.2291	18.93	0.1234	0.4399	45.07
	1.1	24.48	0.5982	0.2193	16.62	0.1132	0.4595	47.27
	1.2	24.17	0.5939	0.2174	15.87	0.1090	0.4698	49.04
	1.3	23.78	0.5880	0.2223	16.72	0.1109	0.4724	50.50
	1.4	23.31	0.5806	0.2323	18.88	0.1178	0.4668	51.73
	1.5	22.79	0.5719	0.2459	22.14	0.1285	0.4541	52.80
$\times 16$	0	21.11	0.4249	0.6201	159.66	0.4152	0.3044	18.69
	1.0	22.16	0.4999	0.3085	30.32	0.1557	0.4604	43.88
	1.1	21.86	0.4971	0.2939	24.14	0.1393	0.4790	46.56
	1.2	21.48	0.4919	0.2905	21.58	0.1334	0.4875	48.65
	1.3	21.01	0.4846	0.2960	22.04	0.1372	0.4848	50.28
	1.4	20.49	0.4754	0.3078	25.01	0.1480	0.4713	51.57
	1.5	19.92	0.4648	0.3235	29.97	0.1632	0.4473	52.61

Ref branch to the noisy tokens in the attention stage is eliminated. As shown in Fig. 5, the resulting images are noticeably blurry and lack high-frequency details, with all metrics substantially worse than the baseline ($\omega = 1.0$). This confirms a significant directional discrepancy between the weakened and normal predictions, which is precisely the prerequisite for autoguidance to be effective.

As illustrated in Fig. 5, appropriately increasing ω within a certain range improves the visual quality of the reconstruction, yielding sharper land cover boundaries and finer details. However, excessively large ω leads to over-sharpening and color distortion, thereby degrading fidelity.

C.2 Comparison with Other Training-Free Guidance Methods

Table 6: Comparison with other training-free guidance methods on SECOND $\times 8$.

Method	LPIPS \downarrow	FID \downarrow	DISTS \downarrow	CLIQQA \uparrow	MUSIQ \uparrow
Baseline (w/o guidance)	0.2291	18.93	0.1234	0.4399	45.07
+ PAG	0.2260	15.89	0.1106	0.4617	50.05
+ SEG	0.2192	15.97	0.1123	0.4597	46.58
+ ICG	0.2205	15.97	0.1135	0.4570	46.51
+ AG (Ours)	0.2174	15.87	0.1090	0.4698	49.04

We further compare the adopted autoguidance (AG) with three representative training-free guidance variants, including PAG [1], SEG [15], and ICG [27].

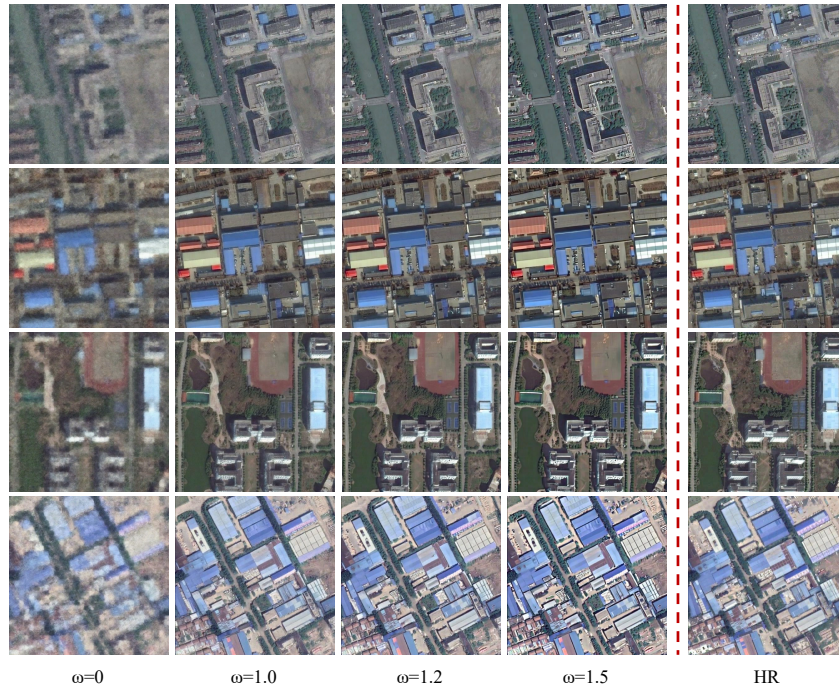


Fig. 5: Impact of different guidance coefficients ω on the SECOND $\times 16$ dataset.

For a fair comparison, the guidance scale of each variant is individually tuned to a competitive value. As shown in Tab. 6, our AG achieves a slight overall advantage over the compared guidance variants.

Training-free guidance methods usually construct a weak or perturbed prediction at inference time, which is not explicitly seen during training. PAG [1] perturbs selected attention maps by replacing them with identity matrices, SEG [15] smooths attention weights via Gaussian blurring, and ICG [27] adopts independent out-of-distribution conditions. Importantly, these weak predictions are not used as standalone reliable outputs, but only to estimate a differential guidance direction. Our AG is in a similar spirit, but is tailored to the RefSR setting. The weak prediction is obtained by suppressing only the reference interaction branch, so it remains anchored to the LR structural prior while reducing the influence of reference information. This allows AG to provide an effective guidance direction without additional training.

D More Qualitative Comparisons

We provide more visual comparisons of different RefSR methods on the SECOND [40] and FUSU [44] datasets to further demonstrate the superiority of our approach. Specifically, Figs. 6 and 7 display the super-resolution results on SEC-

OND $\times 8$ and $\times 16$, respectively, while Figs. 8 and 9 show the results on FUSU $\times 8$ and $\times 16$. As illustrated in these figures, our method consistently achieves superior visual quality across all settings.

E Computational Cost

Table 7: Computational cost for generating a 512×512 image. Runtime is measured on a single NVIDIA A100 GPU.

	Ref-Diff	CoSeR*	Creati*	M ³ -DiT	Ours	Ours (w/ AG)
Params (M)	116.74	2655.50	3629.07	3005.81		3188.56
Steps	40	200	40	40		40
Time (s)	32.93	30.19	2.44	2.22	2.48	4.73
FLOPs (T)	940.63	249.93	93.46	81.85	90.88	181.75

We report the computational cost of diffusion-based RefSR methods when generating a 512×512 image. The runtime is measured on a single NVIDIA A100 GPU. As shown in Tab. 7, when AG is enabled, the inference cost increases because an additional weak prediction is computed for guidance, while the model parameters remain unchanged.

F Limitations

The coefficient ω in autoguidance remains a manually tuned hyperparameter, lacking an adaptive selection mechanism. Moreover, degradations in real-world scenarios are often complex and diverse [9, 21, 35]. Some Real-World Image Super-Resolution (Real-ISR) methods [4, 37, 43] address this issue by training image encoders to extract useful features from degraded inputs. Integrating such strategies with our framework to handle real-world remote sensing scenarios is a promising direction for future work.

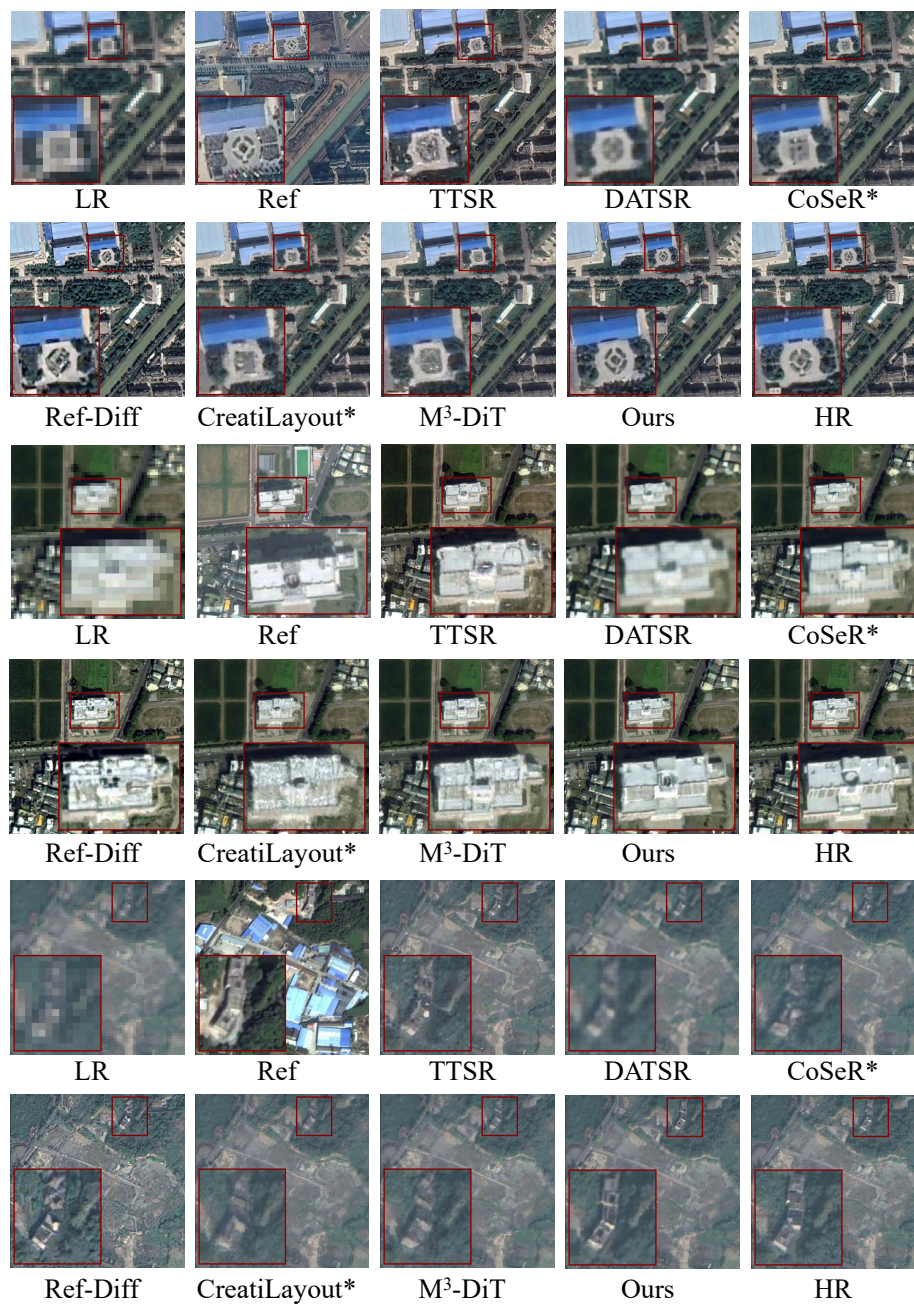


Fig. 6: Qualitative comparison on the SECOND $\times 8$ dataset.

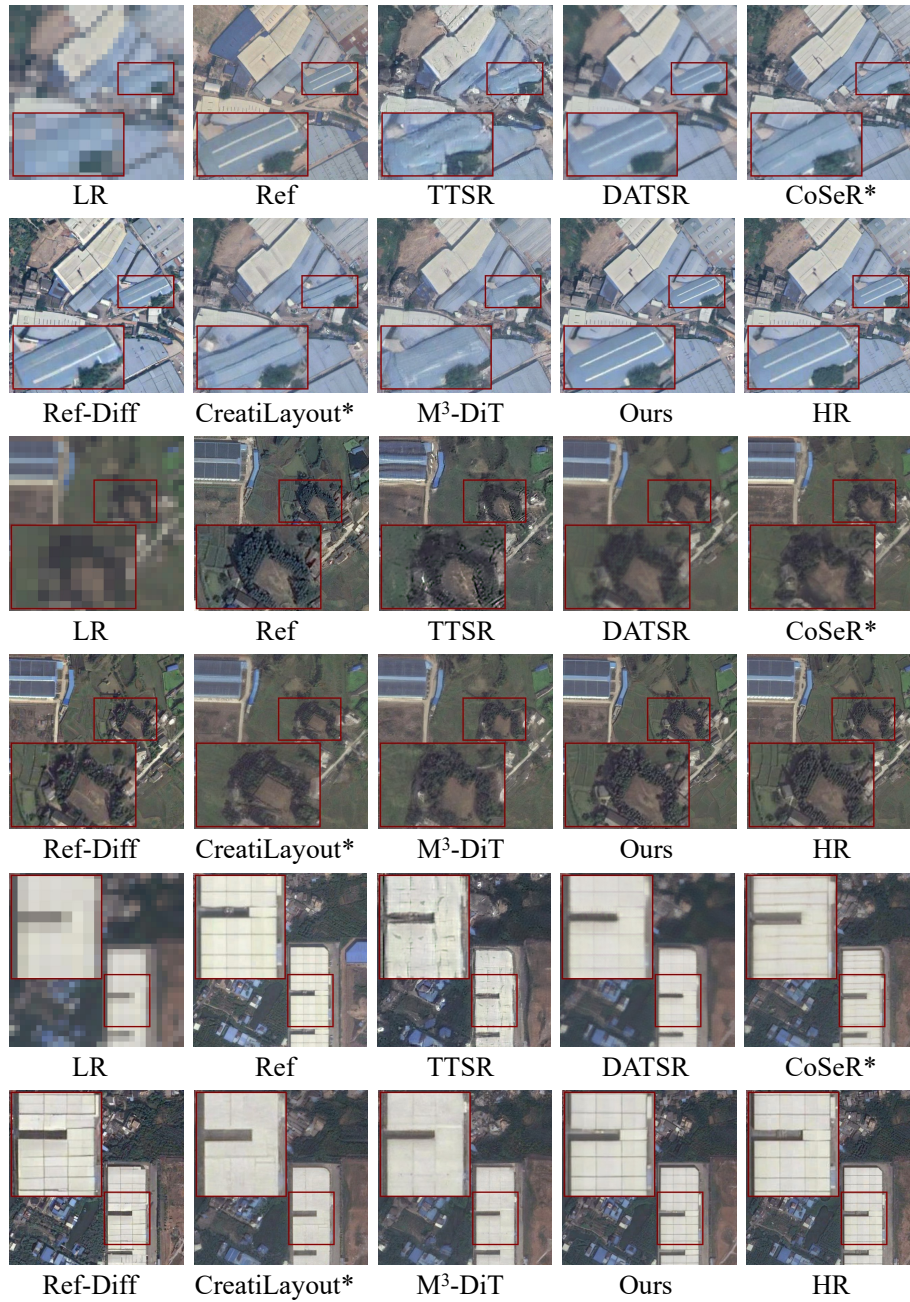


Fig. 7: Qualitative comparison on the SECOND $\times 16$ dataset.

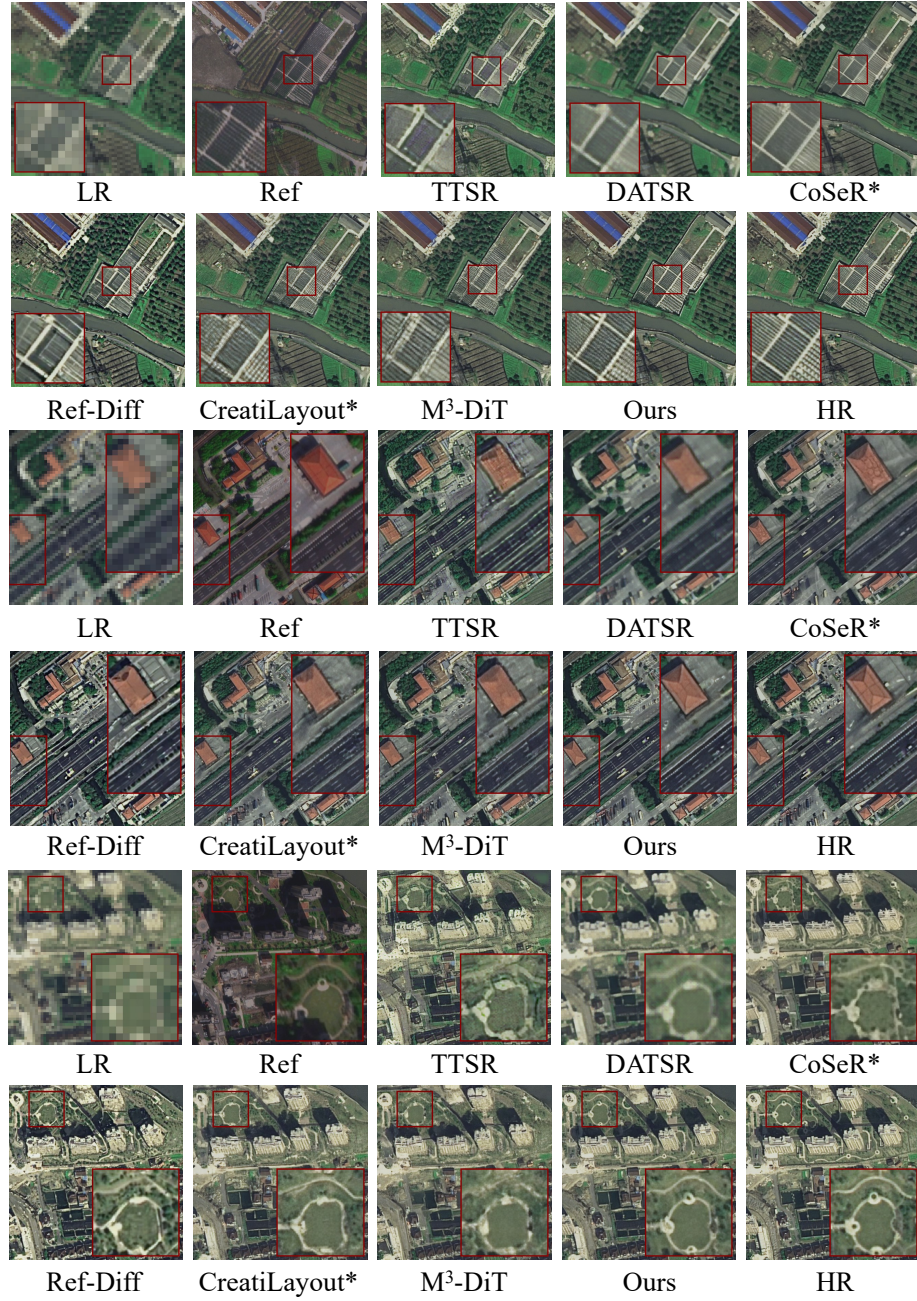


Fig. 8: Qualitative comparison on the FUSU $\times 8$ dataset.

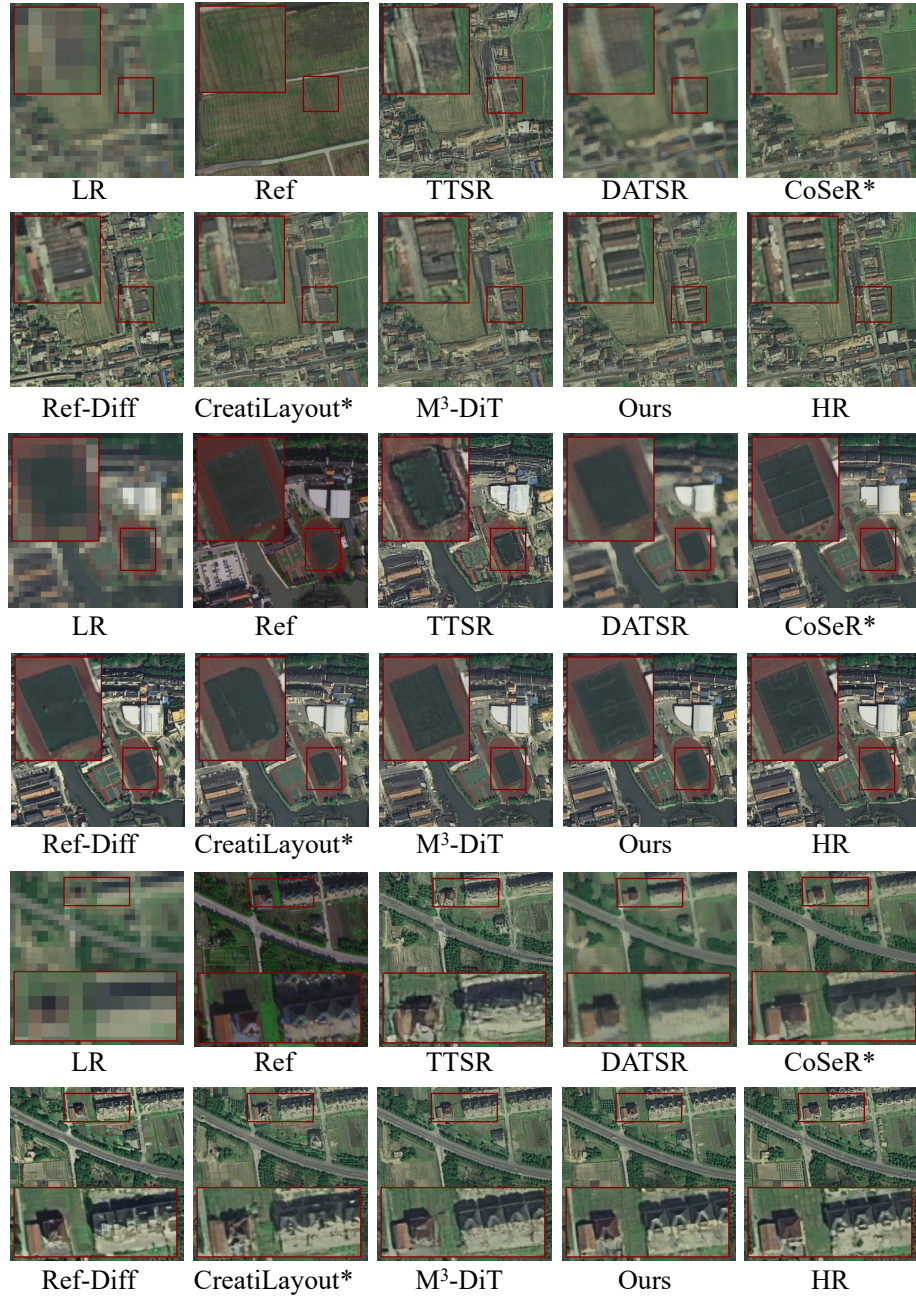


Fig. 9: Qualitative comparison on the FUSU $\times 16$ dataset.